1 **RESEARCH ARTICLE**

2 **TITLE:** H^+/K^+ ion pump enhances cytoskeletal polarity to drive gastrulation in sea

3 urchin embryo

4 **Running title:** H^+/K^+ ion pump and gastrulation

5 Kaichi Watanabe[1,*], Yuhei Yasui[1], Yuta Kurose[2], Masashi Fujii[1], Takashi Yamamoto[1],

6 Naoaki Sakamoto[1,*], Akinori Awazu[1,3,*]

7

8 [1] Graduate School of Integrated Sciences for Life, Hiroshima University, Higashi-

9 Hiroshima, 739-8526, Japan

10 [2] Department of Mathematical and Life Sciences, Graduate School of Science,

11 Hiroshima University, Higashi-Hiroshima, 739-8526, Japan

12 [3] Research Center for the Mathematics on Chromatin Live Dynamics, Hiroshima

13 University, Higashi-Hiroshima, Hiroshima, 739-8526, Japan

14

15 *Corresponding authors (kaichi1849@hiroshima-u.ac.jp (K.W.); naosaka@hiroshima-

16 u.ac.jp (N. S.); awa@hiroshima-u.ac.jp (A. A.))

17

18 **KEY WORDS: Gastrulation, H^+/K^+ ion pump, sea urchin, cytoskeleton, pH**

19 **regulation**

20 **Summary statement:** The H^+/K^+ ion pump is critical for normal gastrulation in

21 sea urchin through pH regulation of cell-position dependent intracellular actin

22 distributions.

23 **ABSTRACT**

24 Gastrulation is a universal process in the morphogenesis of many animal embryos. In

25 sea urchin embryos, it involves the invagination of single-layered vegetal plate

26 into blastocoel. Although morphological and molecular events have been well

27 studied for gastrulation, the mechanical driving forces and their regulatory

28 mechanism underlying the gastrulation is not fully understood. In this study,

29 structural features and cytoskeletal distributions were studied in sea urchin embryo

30 using an "exogastrulation" model induced by inhibiting the H^+/K^+ ion pump with

31 omeprazole. The vegetal pole sides of the exogastrulating embryos had reduced

32 roundness indices, intracellular pH polarization, and intracellular F-actin polarization at

33 the pre-early gastrulation compared with the normal embryo. Gastrulation stopped when

34 F-actin polymerization or degradation was inhibited by *RhoA* or *YAP1* knockout,

35 although pH distributions were independent of such a knockout. A mathematical model

36 of sea urchin embryos at the early gastrulation reproduced the shapes of both normal

37 and exogastrulating embryos using cell-dependent cytoskeletal features based on F-actin

38 and pH distributions. Thus, gastrulation required appropriate cell position-dependent

39 intracellular F-actin distributions regulated by the H^+/K^+ ion pump through pH control.

40

INTRODUCTION

Gastrulation is a universal and essential morphogenic process in various animals, wherein a ball of single layered cells (blastula) differentiates into a multilayered gastrula or early embryo (Serrano Nájera and Weijer, 2020; Shindo, 2018; Stower and Bertocchini, 2017). Species-specific variations in this process provides the basis for particular animal morphologies and leads to the generation of internal organs. The basic mechanism of whole embryonic transformations induced by organizational rearrangements and cell movements are expected to be universal.

Sea urchin embryos are commonly used for studying various morphogenetic processes universally observed in animals, such as the left–right symmetry breakage (Aihara and Amemia, 2001; McCain and McClay, 1994; Takemoto et al., 2016; Warner and McClay, 2014), neural network formations (Burke et al., 2014; McClay et al., 2018; Yaguchi et al., 2010), and gastrulation (Dan and Okazaki, 1956; Gustafson and Kinnander, 1960; Hardin and Cheng, 1986; Kominami and Takata, 2004; Martik and McClay, 2017) due to its evolutionary position as an ancestral deuterostome. Furthermore, the gene regulatory network controlling endomesoderm specification in sea urchin embryo has been well studied (Davidson et al., 2002; Oliveri & Davidson, 2004). Sea urchin gastrulation progresses through the following four steps (Kominami and Takata, 2004): step 1 (after hatching), the embryo becomes an epithelial monolayer with a thickened vegetal pole; step 2 (pre-gastrulation), the vegetal plate bends to invade the blastocoel; step 3 (early gastrulation), the tubular archenteron is formed, and secondary mesenchyme cells (SMCs) appear at the tip; step 4 (mid-late gastrulation),

4

63   the archenteron elongates by pulling on the filopodia of the SMC. Steps 1 and 2 refer to

64   the primary invagination stages, and steps 3 and 4 are those of the secondary

65   invagination stages (Dan and Okazaki, 1956; Gustafson and Kinnander, 1956).

66   The embryos of some sea urchin species exhibit anomalous morphogenesis

67   (exogastrulation) under various perturbations where the vegetal plate of the embryo

68   prolapses outward instead of invaginating. For example, the archenteron of embryos

69   cultured with LiCl or sugar is completely evaginated due to the depolymerization of

70   SMC microtubules in the blastocoel space connecting the primary intestine and

71   ectoderm (Dan and Okazaki, 1956; Hardin and Cheng, 1986; Khurrum et al., 2004).

72   These studies suggest that lifting the primary intestine from the mid-gut by

73   microtubules plays an important role in step 4 of gastrulation. Exogastrulation was also

74   observed by Rab35 knockdown that was also suggested to disturb whole embryonic

75   cytoskeleton distribution (Remsburg et al., 2021).

76   Moreover, bending of the vegetal plate in step 2 of normally cultured embryos of

77   the sea urchin, *Lytechinus pictus* (LP), occurs even when it is surgically isolated

78   (Ettensohn, 1984). It is suggested that the tip of the archenteron should be bottle-shaped

79   (Nakajima and Burke, 1996), and the area around the vegetal plate should be wedge-

80   shaped (Burke et al., 1991) to initiate primary invagination (Kominami and Takata,

81   2004). Additionally, mathematical models of vegetal poles suggest that primary

82   invagination occurs under the appropriate force conditions for "apical constriction,"

83   "cell tractor," "apical contractile ring," "apicobasal contraction," and "gel swelling"

84   (Davidson et al., 1995; Odell et al., 1981). However, it is unclear which of these effects

5

85   are essential for development up to pre-early gastrulation (steps 2 and 3).

86   In this study, the roles of the dominant factors in steps 2 and 3 of gastrulation of sea

87   urchins were determined through experimental analyses and mathematical modeling.

88   First, specific inhibition of H^+/K^+ ion pump activity by omeprazole caused "partial"

89   exogastrulation without the loss of microtubules in the blastocoel space of embryos

90   from the sea urchin, *Hemicentrotus pulcherrimus* (HP). The H^+/K^+ ion pump regulates

91   the pH in cells and pH influences the structure and force of the actomyosin system

92   (Köhler et al., 2012). Therefore, the partial exogastrulation was likely due to anomalous

93   cytoskeletal behaviors. Second, knockout experiments on cytoskeleton-related

94   molecules were performed in HP embryos and analyzed by fluorescence imaging. Third,

95   simulations of morphogenic process of normal and H^+/K^+ ion pump inhibited

96   (exhibiting exogastrulation) HP embryo during the pre-early gastrulation were

97   performed using a mathematical model utilizing the cytoskeletal force parameters

98   determined by the above experiments. The modeled shapes of the H^+/K^+ ion pump-

99   inhibited embryos of the sea urchin, *Lytechinus variegatus* (LV,) were compared to

100   those of HP to reveal the contributions of the H^+/K^+ ion pump to the regulation of

101   cytoskeletal behaviors.

102

103   **RESULTS**

104   **H^+/K^+ ion pump inhibition in HP embryos caused partial exogastrulation**

105   The development of HP embryos exposed to the specific H^+/K^+ ion pump inhibitor,

106   omeprazole, immediately after fertilization exhibited anomalous morphogenesis with

6

107   partial exogastrulation observed at the primary-secondary invagination stages and 36

108   hours post fertilization (hpf) (Fig. 1). Detailed comparisons of the structural features

109   around the vegetal pole between the normal (control) and inhibited embryos at each

110   gastrulation step are as follows. In step 1, control and inhibited embryos exhibited

111   equivalent vegetal pole thickening (18-20 hpf). In step 2, primary invagination occurred

112   in both control and inhibited embryos at the same time. However, intestinal invagination

113   was slightly shallower in the inhibited embryos than in the control embryos (20-22 hpf).

114   In step 3, inhibited embryos did not show further elongation of the archenteron into the

115   blastocoel, and the shape of inhibited embryos elongated along the animal-vegetal axis

116   (22-24 hpf). In step 4 (secondary invagination stage), the outward protrusion of the

117   vegetal pole side was more pronounced in the inhibited embryo (24 hpf). The inhibited

118   embryo had comparatively little elongation of the archenteron into the blastocoel

119   compared to the control embryos. At 36 hpf, "partial" exogastrulation, in which the tip

120   of archenteron folded inward by the normal primary invagination but the remaining part

121   extended outward during the secondary invagination, was observed in the inhibited

122   embryo.

123   The migration of SMCs was observed in the control embryos and in the inhibited

124   embryos (Fig. 2) indicating that filopodia were formed. Previously reported

125   exogastrulation was induced by the loss of pseudopodia (Dan and Okazaki, 1956;

126   Hoshi, 1979; Khurrum et al., 2004), therefore, partial exogastrulation in this report was

127   expected to occur by a different mechanism.

128

129 **H$^+$/K$^+$ ion pump inhibition perturbed whole embryonic pH and cytoskeletal**

130 **distributions**

131 The intracellular distribution of F-actin and pH was analyzed at the primary

132 invagination stage (steps 1 and 2) to reveal the mechanism underlying the

133 morphological changes in the inhibited embryos at the secondary invagination stage

134 (steps 3 and 4), (Fig. 3A, B). F-actin was visualized by fluorescence of actinin-GFP, and

135 intracellular pH was estimated with pH indicator, whose fluorescent intensity increased

136 as pH decreased. The polarity of intracellular F-actin and pH distribution was evaluated

137 by estimating the fluorescence intensities ratio between the apical and basal sides of

138 cells.

139 Similar apical/basal ratio distributions of actinin-GFP intensities were obtained between

140 the control and inhibited embryos, while the ratios gradually increased closer to the

141 vegetal pole in both embryos at step 1 (Fig. 3C, D, Fig. S1A, B). The distribution of the

142 apical/basal ratios of actinin-GFP intensities in step 2 were similar between control and

143 inhibited embryos only in the animal half (Fig. 3E, Fig. S1C). The ratios of the control

144 embryos from the equator to the vegetal pole was larger than that of inhibited embryos,

145 while nearest the vegetal pole, control embryos showed smaller ratio than that of

146 inhibited embryos. Therefore, the formation of an anomalous embryonic shape of

147 inhibited embryos correlated with the deviation of intracellular F-actin polarity in the

148 vegetal half of the embryos in primary invagination.

149   The apical/basal ratio of the pH indicator was greater than one in both control and

150 inhibited embryos in step 2 (Fig. 3F, Fig. S1D, S2) indicating that the pH on the apical

8

151   side of each cell was always lower than that on the basal side. Additionally, this ratio

152   was higher in the vegetal half than that in the animal half in the control embryo, while

153   this pattern disappeared in the inhibited embryo (Fig. 3F, Fig. S2). Thus, the polarity of

154   the pH indicator fluorescent intensities was positively correlated with that of actinin-

155   GFP in whole embryos (Fig. 3E, F).

156   Meanwhile, inhibition of the H^+/K^+ ion pump did not influence the whole

157   embryonic distribution of fibropellin-1 (Fig. 3G, H), a F-actin scaffold in the apical

158   lamina of the apical pole (Burke et al., 1998; Nakajima and Burke, 1996).

159

160   **Gastrulation starts but does not progress in embryos with knocked out**

161   **cytoskeleton regulators**

162   CRISPR-Cas9-mediated knockout of the typical enhancer and repressor of F-actin

163   formation (*RhoA* and *YAP1*) (Beane et al., 2006; Dupont et al., 2011) was performed by

164   microinjection of sgRNAs designed with *Cas9* mRNA (Fig. S3) to elucidate the

165   contribution of F-actin to the gastrulation process. Although the mutation frequencies of

166   *RhoA* and *YAP1* knockout were 55.6% and 77.8%, respectively, and the frameshift rate

167   was 22.3% in either knockout (Fig. S3), the gastrulation stopped at step 2 at the primary

168   invagination stage in either *RhoA* or *YAP1* knockout embryos (Fig. 4A) and normal

169   gastrulation and exogastrulation were not observed. Interestingly, the phenotypes

170   between these gene knockout embryos were similar, although the gene functions are

171   different (Fig. S3). Pigmented cells were observed at 45 hpf indicating that development

172   had not ceased. This showed that primary invagination occurred even in embryos with

9

173 mild perturbation of F-actin function, but subsequent gastrulation processes required

174 appropriate F-actin-derived forces.

175   The whole embryonic distribution of average intensity and apical/basal ratios of the

176 pH indicator was unchanged in *RhoA*-knockout embryos compared with the control, and

177 therefore, perturbation of F-actin polymerization did not affect the pH gradient of the

178 cell (Fig. 4B, C).

179

180 **Mathematical model of embryonic shape formations in early gastrulation**

181 **considering cell-dependent F-actin polarity**

182 A mathematical model of cell motion at the cross section including animal and vegetal

183 poles during steps 1-3 of gastrulation was constructed to examine the influence of

184 intracellular F-actin distribution on the formation of embryonic shapes. The model was

185 constructed based on that of gastrulation in *Nematostella vectensis* (Tamulonis et al.,

186 2011) that consisted of cells constructed by springs and beads circularly connected to

187 form a 2-dimensional cross section of the embryo. The following assumptions were

188 made based on experimentally known facts.

189 I) Each embryo contained three cell types: pigment cells (Takata and Kominami, 2004),

190 wedge cells (Burke at al., 1991), and other cells (Fig. 5). The pigment cells near the

191 entrance to the cavity were assumed to be bottle-shaped (Takata and Kominami, 2004)

192 because of the site-specific force in these cells. This may explain the bending of the

193 vegetal plate occurring in embryos with knocked out F-actin polymerization regulators

194 (Fig. 4), or a surgically removed animal pole (Ettensohn, 1984). The apical length was

195   sufficiently shorter than the basal length and the apical sides of wedge cells were wider

196   than the basal side (Fig. 5A) to form a similar shape to previously observed embryos

197   (Kominami and Takata, 2004).

198   II) The width of the apical and basal sides changes in a cell-dependent manner in

199   control and inhibited embryos due to cytoskeletal forces generated by F-actin. The

200   apical side elongation was expected to correlate with F-actin concentration because

201   higher F-actin concentration was expected to generate stronger cell cortical forces.

202   Thus, the lengths of the apical and basal sides of cells, except pigment cells and wedge

203   cells, were determined based on their apical/basal ratios of actinin-GFP intensities at

204   step 2 (Fig. 5A).

205   III) The cell divisions and 3-dimensional mutual cell invasions mainly contributing to

206   late gastrulation were not included because these processes were rarely observed in

207   early gastrulation (Mizoguchi, 1999). Therefore, the present model described embryo

208   shape dynamics of the control and inhibited embryos as 2-dimensional motions and

209   deformations of the apical and basal sides of 64 cells (Fig. 5A).

210   The simulations showed different shapes (Fig. 5B), although each shape was like

211   that experimentally observed at step 3 (Fig. 1). Similar temporal changes in roundness

212   indices (Fig. 5C) of control embryos (0.85 ~ 0.9) and inhibited embryos (0.75 ~ 0.8)

213   were observed in the simulated data (Fig. 5D, Fig. S4A) and experimental data (Fig. 5E,

214   Fig. S4B).

215   The simulation where the elongation ratio of the apical side of each cell was a little

216   larger than that of control was also performed, with this model named: "over-polarized

11

217   embryo" (Fig. 5A, B). The whole embryonic shape of this model resulted in a wider and

218   larger roundness index than the control embryos (Fig. S4A). This suggested that the

219   apical/basal ratio polarity of F-actin distribution in each cell was sensitive to the whole

220   embryonic shape.

221

222   **DISCUSSION**

223   Inhibition of the H^+/K^+ ion pump resulted in abnormal embryo shape with partial

224   exogastrulation due to intracellular apical F-actin distribution at the vegetal pole (Fig. 3,

225   5). F-actin concentrations generating cell cortical forces were significantly larger at the

226   apical side of each cell than that of the basal side in the vegetal half of the control

227   embryos, except for cells at the vegetal pole. Therefore, the apical planes of wedge cells

228   and other cells in the vegetal pole side were expected to be significantly wider than the

229   basal planes. Conversely, the apical plane of cells in the vegetal half of the inhibited

230   embryo were not significantly wider compared to the basal sides due to lower apical F-

231   actin levels. The simulation results showed that such expected features in the vegetal

232   half may progress to normal early gastrulation in the control embryos and partial

233   exogastrulation in the inhibited embryos (Fig. 5). Therefore, appropriate embryonic

234   intracellular apical F-actin distribution in the vegetal half is required for gastrulation.

235   One recent study suggested an outer intestinal embryo is formed by Rab35

236   knockdown that might disturb the whole embryonic intracellular F-actin polarity

237   (Remsburg et al., 2021). The results of the present study support this suggestion, and

238   further indicate that the intracellular F-actin polarity on the vegetal pole side of the

239   embryo is particularly important for accurate gastrulation and the intracellular pH

240   controlled by H^+/K^+ ion pump is involved in this process.

241   Gastrulation does not proceed when apical lamina is inhibited (Burke et al., 1991).

242   The whole embryonic distributions of apical lamina along cells were nearly identical

243   between the control and inhibited embryos, although large differences were observed

244   between the cell shapes in the vegetal half and whole embryos. This indicated that the

245   generated force was independent of the relative amounts of apical lamina in each cell.

246   Embryos with partial knockout of F-actin regulating factors (*RhoA* or *YAP1*) stopped the

247   gastrulation at the primary invagination step (Fig. 4A, B). This indicated that the

248   seconday invagination is inhibited without appropriately regulated F-actin, even if the

249   apical lamina exists. Therefore, the apical lamina was suggested to be the scaffold for

250   apical F-actin to generate the force required for the deformation processes driving the

251   secondary invagination of gastrulation and whole embryonic deformation.

252   CRISPR-Cas9-mediated *RhoA* knockout showed intermediate level (55.6%) of

253   mutation frequency (Fig. S3) and the knockout embryos exhibited the primary

254   invagination. However, LV embryos expressing dominant negative RhoA failed to

255   initiate primary invagination (Beane et al., 2006). Therefore, contribution of F-actin

256   function is considerable for the primary invagination, but the extent of the dependency

257   on F-actin function is less and a mechanism other than the F-actin-related system might

258   be involved in this initial process. As mentioned above, F-actin function must be

259   essential for the secondary invagination.

260   The F-actin network formation generating cell cortical forces was drastically

13

261 enhanced with decreased pH *in vitro* (Köhler et al., 2012) (25). The lower pH at the

262 apical side compared with the basal side was maintained by H^+/K^+ ion pump activity.

263 Whole embryonic distributions of apical/basal ratios of pH indicator at step 2 correlated

264 with those of intracellular actinin-GFP (Fig. 3D, F) suggesting that the F-actin

265 concentration was high when the pH was low at the apical side of cells. Additionally,

266 the apical/basal F-actin polarity in each cell significantly decreased in the vegetal half of

267 the embryo by inhibiting H^+/K^+ ion pump activity (Fig. 3E). Conversely, the whole

268 embryonic distribution of intracellular pH and polarity was unchanged even when F-

269 actin polymerization was directly perturbed by knockout of F-actin regulating factors

270 (Fig. 4D). This suggested that the intracellular pH controlled by the H^+/K^+ ion pump is a

271 one-sided regulator of F-actin polymerization.

272   Inhibition of the H^+/K^+ ion pump did not influence on the whole embryonic

273 distribution of the apical lamina (Fig. 3G, H). This suggested that the regulation of F-

274 actin intracellular distribution by pH is independent of the apical lamina. The embryo

275 exhibited partial exogastrulation if the intracellular pH polarity at the primary

276 invagination stage was weaken by inhibiting H^+/K^+ ion pump activity. This indicated

277 that H^+/K^+ ion pump activity in the primary invagination stage provided a dominant

278 contribution to the progress of the normal secondary invagination to form appropriate

279 intracellular F-actin polarity in the whole embryo.

280   The influence of pH on F-actin network formation and force generation is a

281 universal biochemical feature confirmed by *in vitro* experiments (Köhler et al., 2012).

282 Inhibition of H^+/K^+ ion pump activity significantly decreases intracellular pH in the LV

14

283   embryo (Schatzberg et al., 2015), while an increase in the intracellular pH was observed

284   in the majority of cells in the HP embryo (Fig. S5). Decreases in the intracellular pH of

285   LV may induce increases in the apical/basal polarities of intracellular pH and F-actin

286   concentration like the "over-polarized embryo" model. The over-polarized embryo

287   model exhibited a wider embryonic shape with a larger roundness index than the control

288   embryos (Fig. 5B, S4B) which is consistent with LV imaging (Schatzberg et al., 2015).

289   This supported the suggestion that H^+/K^+ ion pump activity significantly contributed to

290   early gastrulation through the regulation of intracellular F-actin apical/basal

291   polarizations.

292   Omeprazole treatment of sea urchin embryos disrupts the left-right asymmetric

293   formations of the adult rudiment although gastrulation is completed (Bessodes et al.,

294   2012; Duboc et al., 2005; Hibino et al., 2006). The left-right asymmetric *nodal* gene

295   expression observed immediately after gastrulation is important for establishing this

296   asymmetry (Duboc et al., 2005). Frogs, chickens, zebrafish, and ascidians disrupt left-

297   right asymmetry by inhibiting H^+/K^+ ion pump activity (Kawakami et al., 2005; Levin

298   et al., 2002; Shimeld and Levin, 2006). Disrupted left-right asymmetry in HP is

299   observed at lower (~ 3/5 times) omeprazole concentrations (Hibino et al., 2006) than

300   those in this study. Inhibition of H^+/K^+ pump activity by dilute omeprazole solutions

301   induced weak perturbation of gut formation in this study, which may disrupt cell-cell

302   interactions and regulate whole embryonic *nodal* gene expression.

303   This report revealed the close relationship between pH, F-actin, and H^+/K^+ ion

304   pump activity inducing normal/abnormal gastrulation in sea urchins through

15

305   intracellular F-actin regulation. Embryonic F-actin distribution on the apical side of

306   each cell was important for normal gastrulation, and H^+/K^+ ion pump activity may be

307   involved in F-actin distribution. This finding provides key insights into the evolutionary

308   relationship between development and morphogenesis. Intracellular apical/basal

309   polarity of pH showed different cellular features between vegetal and animal poles in

310   step 2 of gastrulation. However, the formation of these position-dependent intracellular

311   states was not explored. Therefore, upstream regulators of H^+/K^+ ion pump activity

312   should be investigated to reveal the detailed morphogenesis molecular mechanism. The

313   universal effect of inhibiting H^+/K^+ ion pump activity on early embryo formation among

314   different animals will be tested in the future.

315

316   **MATERIALS AND METHODS**

317   **Animals and embryos**

318   Adult Japanese sea urchins (HP) were collected from Seto Inland Sea or Tateyama Bay.

319   Eggs and sperm were obtained by coelomic injection of 0.55 M KCl. Fertilized eggs

320   were cultured in filtered seawater at 16°C.

321

322   **Inhibition of H^+/K^+ ion pump by omeprazole**

323   A 100 mM stock solution of omeprazole (FUJIFILM Wako Pure Chemical Corporation,

324   Japan) dissolved in dimethyl sulfoxide (DMSO) was immediately added to fertilized

325   eggs to a final concentration of 100 μM and cultured at 16°C.

326

327   *In situ* **nucleus and F-actin visualization in embryos**

328   Sea urchin embryos were fixed by immersion in fixative III (4% paraformaldehyde,

329   32.5% filtered seawater, 32.5 mM 3-(N-morpholino)propane sulfonic acid (MOPS), pH

330   7.0, 162.5 mM NaCl) for 16 h at 4°C. Embryos were washed three times using 0.5 mL 1

331   x phosphate buffered saline (PBS), stored in 100% ethanol at -20°C, and used within 1

332   week. Fixed embryos were washed three times with 1 x PBS, permeabilized with 0.5%

333   Triton X-100 for 20 min at room temperature, washed three times with 1 x PBS, and

334   stained with 100 nM phalloidin (in 1 x PBS) for 45 min at room temperature. Stained

335   embryos were washed three times with 1 x PBS, mounted in SlowFade Gold antifade

336   mountant with DAPI (Molecular Probes) and observed using a confocal laser scanning

337   microscopy (Carl Zeiss LSM 700, Germany) with laser illumination at 405/435 nm

338   excitation/emission for DAPI and 555/573 nm excitation/emission for phalloidin,

339   respectively.

340

341   **Live imaging of pH, actinin, and apical lamina**

342   Intracellular pH of sea urchin embryos was visualized using pHrodo Red AM

343   intracellular pH indicator or 5-(and-6)-carboxy SNARF-1 (C-1270) (ThermoFisher

344   Scientific, USA) at final concentrations of 10 µM and 5 µM, respectively, and stained at

345   16°C for 30 min. The embryos were washed in filtered seawater and observed using

346   confocal microscopy with laser illumination at 555/585 nm excitation/emission for

347   pHrodo and 555/573 m excitation/emission for SNARF-1, respectively.

17

348   Actinin and fibropellin-1 were visualized following fusion of the proteins with GFP.

349   RNA was extracted from mesenchyme blastula stage HP embryos using ISOGEN

350   (Nippongene, Japan) according to the manufacturer's instructions. Actinin and

351   fibropellin-1 coding sequences were amplified by RT-PCR using SuperScript™ III

352   Reverse Transcriptase (Thermo Fisher Scientific, USA) with the primers stated in Table

353   S1 and cloned into pGreenLantern2-derived plasmid at restriction sites EcoRI and

354   XhoI. mRNA (actinin-GFP, fibropellin-1-GFP, in that order) was synthesized *in vitro*

355   using an mMESSAGE mMACHINE T7 ultra transcription kit (ThermoFisher Scientific,

356   USA) and purified using an RNeasy mini kit (Qiagen, Nederland). mRNA was

357   microinjected into fertilized eggs as described by Liu et al., (2019).

358   Fluorescent images were acquired by confocal microscopy using an excitation of

359   488 nm, and emission of 515 nm. The images of the animal and vegetal poles of the

360   embryo were analyzed based on the *z*-stack image with the largest area by averaging

361   seven *z*-axis images with a total thickness of 6 µm.

362

363   **Quantification of experimental images**

364   The fluorescent images of embryos were acquired according to the angle θ (0°~180°)

365   between the vegetal and animal poles along the circumference (Fig. S6) and

366   transformed into a band-like image using the "Polar Transformer" function

367   (https://imagej.nih.gov/ij/plugins/polar-transformer.html) of ImageJ 2.1.0. Each band-

368   like image was filtered using a median filter (radius = 1.0). The filtered images were

369   binarized using "Mean" (pHrodo indicator), "IsoData" (actinin), and "Triangle"

18

370 (fibropellin-1 and SNARF-1) functions, respectively, to obtain the cellular regions of

371 the embryo. The apical/basal ratios of the pH indicator, actin-GFP, and fibropellin-1-

372 GFP for θ were determined using average fluorescent intensities over the regions with

373 the width of 3.126 μm from the apical and basal sides.

374 The fluorescent intensity of the pHrodo indicator was defined by the average

375 fluorescent intensity over the intracellular region with a width of 6.232 μm from the

376 apical side (Fig. S6). Fluorescent values were estimated by taking the ratio between the

377 observed fluorescence intensity and the average background fluorescence intensity

378 around the entire embryo.

379 F-actin and apical lamina were stained by mRNA microinjections of actinin-GFP

380 and fibropellin-1-GFP to fertilized eggs. Nonnegligible variations was inevitable in the

381 concentration of injected mRNA among fertilized egg samples, which would be

382 amplified during development. Therefore, only the apical/basal ratios were used to

383 evaluate the intracellular features of F-actin and apical lamina distributions.

384 Two data points were obtained for each θ from each fluorescence image of the

385 embryo since the left and right sides of the embryo were considered axis symmetric

386 against the animal-vegetal axis. Both data were used to estimate the sample average and

387 95% confidence interval of each value, where the number of samples (n) was given by 2

388 × [number of observed embryos].

389

390 **Gene knockout by CRISPR-Cas9**

391 Knock out of endogenous *RhoA* and *YAP1* in HP was performed using the method

19

392   described by Liu et al., (2019). The oligonucleotide sequences used in sgRNA

393   preparations were listed in Table S2.

394

395   **Heteroduplex mobility assay (HMA) and DNA sequencing analysis**

396   Analysis of knockout embryos by HMA and DNA sequencing was performed according

397   to Liu et al., (2019). The primer sequences used to amplify each target region were

398   listed in Table S3.

399

400   **Mathematical model of sea urchin embryos**

401   A 2-dimensional particles model describing cellular motion at the cross section of

402   animal poles and vegetal poles of sea urchin embryos during steps 1 to 3 of gastrulation

403   was constructed. The determined number of cells was based on that at the equatorial

404   plane of the embryo at the blastula stage (Mizoguchi, 1999). The following assumptions

405   were made: 1) each cell was represented by 16 particles with radii (r) of 1.125 μm, and

406   each embryo was represented by 64 cells connected in a ring (Fig. S7). 2) Each cell

407   perimeter was 36 μm and the height and width of the embryo at step 1 was 110 μm and

408   100 μm, respectively, which was consistent with sea urchin embryo observations

409   (results not shown). 3) The number of cells was constant because cell divisions and

410   cell invasions from other cross-sections were rarely observed during the primary

411   invagination stage (Mizoguchi, 1999). 4) The motion of each particle obeyed the

412   following overdamped limit of the equation of motion:

413 $\quad \frac{\partial X_{i,j}}{\partial t} = -\frac{1}{\gamma}\frac{\partial V}{\partial X_{i,j}}$ $\qquad$ (1),

414 $\quad$ where $\boldsymbol{X_{i,j}} = (x_{i,j}(t), y_{i,j}(t))$ is the position of the j-th particle constructing the i-th

415 $\quad$ cell ($i = 0,1,2...63$ and $j = 0,1,2...15$) on the x–y plane at time t (Fig. 5, Fig. S7), γ is the

416 $\quad$ coefficient of the drag force acting on each particle, and V is the potential of the entire

417 $\quad$ system. 5) The y-axis was parallel to the animal-vegetal axis of the embryo model. We

418 $\quad$ rewrote $\frac{V}{\gamma} = U$ and U was calculated by:

419 $\quad U = U_{bond} + U_{collision} + U_{actin} + U_{adhesion} + U_{ca} + U_{ea}$ $\qquad$ (2),

420 $\quad$ where U_{bond} is the elastic force potential between each neighboring pair of particles in

421 $\quad$ each cell to maintain each cell perimeter, denoted by:

422 $\qquad U_{bond} = \sum_{i=0}^{63}\sum_{j=0}^{15}\frac{k_b}{2}(d_{(i,j),(i,j+1)} - 2r)^2$ $\qquad$ (3),

423 $\quad$ where k_b, $d_{(i,j),(i,j+1)}$, and r are the coefficient of elasticity, the distance between the j-

424 $\quad$ th and j +1-th particle ($j + 1 = 0$ for $j = 15$) in the i-th cell at time t, and the particle

425 $\quad$ radius, respectively.

426 $\quad U_{collision}$ is the potential of excluded volume effects among all particles denoted as

427 $\quad$ follows:

428 $\quad U_{collision} = \sum_{i<k}\sum_{j<l}\theta(2r - d_{(i,j),(k,l)})\frac{k_c}{2}(2r - d_{(i,j),(k,l)})^2$ $\qquad$ (4),

429 $\quad$ where k_c is the coefficient of repulsion between two particles, and $\theta(x)$ is the

430 $\quad$ Heaviside step function.

431 $\quad U_{actin}$ is the elastic force potential to form and sustain cell shape with the expansion

432 $\quad$ and contraction of the apical and basal sides by the cytoskeleton denoted as follows:

21

433    $U_{actin} = \sum_i \frac{k_a}{2}((d_{(i,10),(i,14)} - l_i^a)^2 + (d_{(i,2),(i,6)} - l_i^b)^2)$ (5),

434   where the apical and basal sides of the i-th cell consisted of particles with $j = 10 - 14$

435   and $j = 2 - 6$, respectively. The wideness of the apical and basal sides at time t were

436   given by $d_{(i,10),(i,14)}$ and $d_{(i,2),(i,6)}$, respectively. The basic wideness of the apical and

437   basal sides were given by l_i^a and l_i^b, respectively. k_a was assumed by the coefficient

438   of elasticity to sustain the wideness of the apical and basal sides of the cell.

439    $U_{adhesion}$ is the potential force for cell adhesion by proteins such as cadherin, and is

440   denoted as follows:

441    $U_{adhesion} = \sum_i \sum_j \frac{k_h}{2}(d_{(i,j),(i+1,k(j))} - 2r)^2$ (6),

442   where k_h is the coefficient for the adhesive forces between the particles of the i-th and

443    $i + 1$-th cells ($i + 1 = 0$ for $i = 63$), and $k(j) \equiv 6, 7, 8, 9, 10$ for $j \equiv 2, 1, 0, 15, 14$,

444   respectively (Fig. S7).

445   U_{ca} is the potential of the forces to conserve each cell area denoted as follows:

446    $U_{ca} = \sum_i \frac{k_{ca}}{2}(s_i - s_i^{ini})^2$ (7),

447   where k_{ca} is the coefficient of elasticity required to maintain each cell area. The area

448   of the i-th cell was estimated by $s_i = \sum_{j=0}^{15}|X_{i,j} - X_i^{cc}|$ with $X_i^{cc} = \frac{1}{16}\sum_{j=0}^{15} X_{i,j}$, and

449   s_i^{ini} referred to s_i given by $X_{i,j}$ at the initial state.

450   U_{ea} is the potential of the forces to maintain the area (volume) of the sea urchin

451   embryo and denoted as follows:

452    $U_{ea} = \frac{k_{ea}}{2}(S - S^{ini})^2$ (8),

22

453   where k_{ea} is the coefficient of elasticity required to maintain embryo area. The area

454   was estimated by $S = \sum_{i=0}^{63}|X_i^{cc} - X^{ec}|$ with $X^{ec} = \frac{1}{64}\sum_{i=0}^{63}X_i^{cc}$, and S^{ini} referred to

455   S given by $X_{i,j}$ at the initial state.

456   U_{ca} and U_{ea} were considered the alternatives of the volume-conserving forces in real

457   3-D cells and embryos as internal pressures in each cell and embryo are considered

458   isotropic.

459

460   **Simulation method of mathematical model**

461   The simulations of the present mathematical model were performed through the

462   integrals of equation of motion (1) using Euler method with time intervals of 0.000064

463   h with conserved $X^{ec} = (0,0)$. In all models, the parameters

464   $k_{bond}, k_{collision}, k_{actin}, k_{adhesion}, k_{ca}$, and k_{ea} were given empirically as 9375, 6250,

465   8125, 8125, 625, and 0.00625 hour^{-1}, respectively, because there were no experiments to

466   measure or estimate them. The qualitative features of the results were independent of

467   the details of these values if the order was maintained. The model formed the embryo

468   shape at step 1 of gastrulation if the appropriate cell type-dependent values of l_i^a and

469   $l_i^b, = l_i^{a,ini}$ and $l_i^{b,ini}$ were given for the models of pigment cells, wedge cells, and

470   other cells (Fig. 5). This configuration gave the particle positions $X_{i,j}$ at time t = 0

471   (initial configuration) in all simulations.

472   The early gastrulation processes were simulated by the change in l_i^a and l_i^b

473   respectively, from $= l_i^{a,ini}$ and $l_i^{b,ini}$ to $= l_i^{a,fin}$ and $l_i^{b,fin}$ at time $t = 0$. Here, $l_i^{a,fin}$

23

474   and $l_i^{b,fin}$ were assumed to obey $l_i^{a,fin} + l_i^{b,fin} = l_i^{a,ini} + l_i^{b,ini} =$ constant among cells

475   except pigment cells based on the expectation that F-actin was constant. The model

476   showed similar structural behaviors to the early gastrulation as the relaxation process of

477    $d_{(i,10),(i,14)} \rightarrow l_i^{a,fin}$ and $d_{(i,2),(i,6)} \rightarrow l_i^{b,fin}$.

478

479   **Statistical analysis**

480   All experiments were performed independently 2 times or more with 4 replicates or

481   more per experiment. Statistical test was performed using SciPy library

482   (https://www.scipy.org/). The roundness index of the vegetal side of each embryo was

483   evaluated by: [embryo width half-way between the bottom and middle of the

484   embryo]/[embryo length] (Fig. 5C).

485

486

487   **Acknowledgements**

488   We thank Prof. Masato Kiyomoto (Tateyama Marine Laboratory, Ochanomizu

489   University) for supplying live sea urchins. We would like to thank Editage

490   (www.editage.com) for English language editing.

491

492

493   **Competing interests**

494   No competing interests declared.

495

496 **Author Contributions**

497 K.W., N.S., and A.A. conceived and designed the study; K.W., Y.K., and N.S. conducted

498 the experiments; K.W., Y.Y., M.F., and A.A. analyzed the data; K.W. and A.A.

499 conducted the mathematical model construction and simulations; K.W., N.S., and A.A.

500 wrote the manuscript with support from all authors; T.Y. supervised the work.

501

509

510 **References**

511 **Aihara M. and Amemiya, S.** (2001). Left-right positioning of the adult rudiment in sea

512 urchin larvae is directed by the right side. *Development* **128**(24), 4935-4948.

513 doi:10.1242/dev.128.24.4935

514 **Beane, W. S., Gross, J. M. and McClay, D. R.** (2006). RhoA regulates initiation of

515 invagination, but not convergent extension, during sea urchin gastrulation. *Dev.*

516 *Biol.* **292**(1), 213-225. doi:10.1016/j.ydbio.2005.12.031

517 **Bessodes, N., Haillot, E., Duboc, V., Röttinger, E., Lahaye, F. and Lepage, T.**

25

518   (2012). Reciprocal signaling between the ectoderm and a mesendodermal left-

519   right organizer directs left-right determination in the sea urchin embryo. *PLoS*

520   *Genet*. **8**(12), e1003121. doi:10.1371/journal.pgen.1003121

521   **Burke, R. D., Lail, M. and Nakajima, Y.** (1998). The apical lamina and its role in cell

522   adhesion in sea urchin embryos. *Cell Adhesion Comm*. **5**(2), 97-108.

523   doi:10.3109/15419069809040284

524   **Burke, R. D., Moller, D. J., Krupke, O. A. and Taylor, V. J.** (2014). Sea urchin

525   neural development and the metazoan paradigm of neurogenesis. *Genesis* **52**(3),

526   208-221. doi:10.1002/dvg.22750

527   **Burke, R. D., Myers, R. L., Sexton, T. L. and Jackson, C.** (1991). Cell movements

528   during the initial phase of gastrulation in the sea urchin embryo. *Dev. Biol*.

529   **146**(2), 542-557. doi:10.1016/0012-1606(91)90255-2

530   **Dan, K. and Okazaki, K.** (1956). Cytoembryological studies of sea urchins: III. Role

531   of the secondary mesenchyme cells in the formation of the primitive gut in sea

532   urchin larvae. *Biol. Bull.* **110**, 29-42.

533   **Davidson, E. H., Rast, J. P., Oliveri, P., Ransick, A., Calestani, C., Yuh, C. H.,**

534   **Minokawa, T., Amore, G., Hinman, V., Arenas-Mena, C., Otim, O., Brown,**

535   **C. T., Livi, C. B., Lee, P. Y., Revilla, R., Schilstra, M. J., Clarke, P. J., Rust,**

536   **A. G., Pan, Z., Arnone, M. I., Rowen, L., Cameron, R. A., McClay, D. R.,**

537   **Hood, L. and Bolouri, H.** (2002). A provisional regulatory gene network for

538   specification of endomesoderm in the sea urchin embryo. *Dev. Biol.*, **246**(1), 162-

539   190. doi: 10.1006/dbio.2002.0635

540   **Davidson, L. A., Koehl, M. A., Keller, R. and Oster, G. F.** (1995). How do sea

541   urchins invaginate? Using biomechanics to distinguish between mechanisms of

542   primary invagination. *Development* **121**(7), 2005-2018.

543   doi:10.1242/dev.121.7.2005

544   **Duboc, V., Röttinger, E., Lapraz, F., Besnardeau, L. and Lepage, T.** (2005). Left-

545   right asymmetry in the sea urchin embryo is regulated by nodal signaling on the

546   right side. *Dev. Cell.* **9**(1), 147-158. doi:10.1016/j.devcel.2005.05.008

547   **Dupont, S., Morsut, L., Aragona, M., Enzo, E., Giulitti, S., Cordenonsi, M.,**

548   **Zanconato, F., Le Digabel, J., Forcato, M., Bicciato, S. et al.** (2011). Role of

549   YAP/TAZ in mechanotransduction. *Nature* **474**(7350), 179-183.

550   doi:10.1038/nature10137

551   **Ettensohn, C. A.** (1984). Primary invagination of the vegetal plate during sea urchin

552   gastrulation. *Amer. Zool.* **24**(3), 571-588. doi:10.1093/icb/24.3.571

553   **Gustafson, T. and Kinnander, H.** (1956). Microaquaria for time-lapse

554   cinematographic studies of morphogenesis in swimming larvae and observations

555   on sea urchin gastrulation. *Exp. Cell Res*. **11**(1), 36-51. doi:10.1016/0014-

556   4827(56)90188-4

557   **Gustafson, T. and Kinnander, H.** (1960). Cellular mechanisms in morphogenesis of

558   the sea urchin gastrula: The oral contact. *Exp. Cell Res.* **21**(2), 361-373.

559   doi:10.1016/0014-4827(60)90268-8

560   **Hardin, J. D. and Cheng, L. Y.** (1986). The mechanisms and mechanics of

561   archenteron elongation during sea urchin gastrulation. *Dev. Biol*. **115**(2), 490-

562   501. doi:10.1016/0012-1606(86)90269-1

563   **Hibino, T., Ishii, Y., Levin, M. and Nishino, A.** (2006). Ion flow regulates left-right

564   asymmetry in sea urchin development. *Dev. Genes Evol.* **216**(5), 265-276.

565   doi:10.1007/s00427-005-0051-6

566   **Hoshi, M.** (1979). Exogastrulation induced by heavy water in sea urchin larvae. *Cell*

567   *Differ.* 8(6), 431-5. doi:10.1016/0045-6039(79)90039-3

568   **Kawakami, Y., Raya, Á., Raya, R. M., Rodríguez-Esteban, C. and Izpisúa**

569   **Belmonte, J. C.** (2005). Retinoic acid signalling links left-right asymmetric

570   patterning and bilaterally symmetric somitogenesis in the zebrafish embryo.

571   *Nature* **435**(7039), 165-171. doi:10.1038/nature03512

572   **Khurrum, M., Hernandez, A., Eskalaei, M., Badali, O., Coyle-Thompson, C. and**

573   **Oppenheimer, S. B.** (2004). Carbohydrate involvement in cellular interactions in

574   sea urchin gastrulation. *Acta Histochem.* **106**(2), 97-106. doi:

575   10.1016/j.acthis.2004.01.001

576   **Kimberly, E. L. and Hardin, J.** (1998). Bottle cells are required for the initiation of

577   primary invagination in the sea urchin embryo. *Dev. Biol.* **204**(1), 235-50.

578   doi:10.1006/dbio.1998.9075

579   **Köhler, S., Schmoller, K. M., Crevenna, A. H., Bausch, A. R.** (2012). Regulating

580   contractility of the actomyosin cytoskeleton by pH. *Cell Rep.* **2**(3), 433-439.

581   doi:10.1016/j.celrep.2012.08.014

582   **Kominami, T. and Takata, H.** (2004). Gastrulation in the sea urchin embryo: A model

583   system for analyzing the morphogenesis of a monolayered epithelium. *Dev.*

584   *Growth Differ.* **46**(4), 309-326. doi:10.1111/j.1440-169x.2004.00755.x

585   **Levin, M., Thorlin, T., Robinson, K. R., Nogi, T. and Mercola, M**. (2002).

586   Asymmetries in H^+/K^+-ATPase and cell membrane potentials comprise a very

587   early step in left-right patterning. *Cell* **111**(1), 77-89. doi:10.1016/S0092-

588   8674(02)00939-X

589   **Liu, D., Awazu, A., Sakuma, T., Yamamoto, T. and Sakamoto, N.** (2019).

590   Establishment of knockout adult sea urchins by using a CRISPR-Cas9 system.

591   *Dev. Growth Differ*. **61**(6), 378-388. doi:10.1111/dgd.12624

592   **Martik, M. L. and McClay, D. R.** (2017). New insights from a high-resolution look at

593   gastrulation in the sea urchin, *Lytechinus variegatus*. *Mech. Dev.* **148**, 3-10.

594   doi:10.1016/j.mod.2017.06.005

595   **McCain, E.R. and McClay, D.R.** (1994). The establishment of bilateral asymmetry in

596   sea urchin embryos. *Development* **120**(2), 395-404. doi:10.1242/dev.120.2.395

597   **McClay, D. R., Miranda, E. and Feinberg, S. L.** (2018). Neurogenesis in the sea

598   urchin embryo is initiated uniquely in three domains. *Development* **145**(21),

599   dev167742. doi: 10.1242/dev.167742

600   **Mizoguchi, H.** (1999). Cell numbers in the gut of the embryo of the sea urchin

601   *Hemicentrotus pulcherrimus*. *Zool. Sci*. **16**(2), 341-344. doi:10.2108/zsj.16.341

602   **Nakajima, Y. and Burke, R. D.** (1996). The initial phase of gastrulation in sea urchins

603   is accompanied by the formation of bottle cells. *Dev. Biol.* **179**(2), 436-446.

604   doi:10.1006/dbio.1996.0273

605   **Odell, G. M., Oster, G., Alberch, P. and Burnside, B.** (1981). The mechanical basis

606   of morphogenesis. I. Epithelial folding and invagination. *Dev. Biol*. **85**(2), 46-62.

607   doi:10.1016/0012-1606(81)90276-1

608   **Oliveri, P. and Davidson, E. H.** (2004). Gene regulatory network controlling

609   embryonic specification in the sea urchin. *Curr. Opin. Genet. Dev*., **14**(4), 351–

610   360. doi: 10.1016/j.gde.2004.06.004

611   **Remsburg, C., Testa, M., Song, J. L.** (2021). Rab35 regulates skeletogenesis and

612   gastrulation by facilitating actin remodeling and vesicular trafficking. *Cells &*

613   *Dev.*, **165**(3), 203660. doi: 10.1016/j.cdev.2021.203660

614   **Schatzberg, D., Lawton, M., Hadyniak, S. E., Ross, E. J., Carney, T., Beane, W. S.,**

615   **Levin, M. and Bradham, C. A.** (2015). H^+/K^+ ATPase activity is required for

616   biomineralization in sea urchin embryos. *Dev. Biol.* **406**(2), 259-270.

617   doi:10.1016/j.ydbio.2015.08.014

618   **Serrano Nájera, G. and Weijer, C. J.** (2020). Cellular processes driving gastrulation

619   in the avian embryo. *Mech. Dev*. **163**, 103624. doi:10.1016/j.mod.2020.103624

620   **Shimeld, S. M. and Levin, M.** (2006). Evidence for the regulation of left-right

621   asymmetry in *Ciona intestinalis* by ion flux. *Dev. Dyn*. **235**(6), 1543-1553.

622   doi:10.1002/dvdy.20792

623   **Shindo, A.** (2018). Models of convergent extension during morphogenesis. (2018).

624   *WIREs Dev. Biol*. **7**(1), e293. doi:10.1002/wdev.293

625   **Stower, M. J. and Bertocchini, F.** (2017). The evolution of amniote gastrulation: the

626   blastopore-primitive streak transition. *Wiley Interdiscip. Rev. Dev. Biol*. **6**(2),

627   e262. doi: 10.1002/wdev.262

628   **Takata, H. and Kominami, T.** (2004). Pigment cells trigger the onset of gastrulation in

629   tropical sea urchin *Echinometra mathaei*. *Dev. Growth Differ*. **46**(1), 23-35.

630   doi:10.1111/j.1440-169X.2004.00726.x

631   **Takemoto, A., Miyamoto, T., Simono, F., Kurogi, N., Shirae-Kurabayashi, M.,**

632   **Awazu, A., Suzuki, K.-i. T. and Sakamoto, N.** (2016). Cilia play a role in

633   breaking left-right symmetry of the sea urchin embryo. *Genes Cells* **21**(6), 568-

634   578. doi:10.1111/gtc.12362

635   **Tamulonis, C., Postma, M., Marlow, H. Q., Magie, C. R., de Jong, J. and**

636   **Kaandorp, J.** (2011). A cell-based model of *Nematostella vectensis* gastrulation

637   including bottle cell formation, invagination and zippering. *Dev. Biol.* **351**(1),

638   217-228. doi:10.1016/j.ydbio.2010.10.017

639   **Voiculescu, O., Bodenstein, L., Lau, I. J. and Stern, C. D.** (2014). Local cell

640   interactions and self-amplifying individual cell ingression drive amniote

641   gastrulation. *eLife* **3**, e01817. doi: 10.7554/eLife.01817

642   **Warner, J. F. and McClay, D. R.** (2014). Left-right asymmetry in the sea urchin.

643   *Genesis* **52**(6), 481-487. doi:10.1002/dvg.22752

644   **Yaguchi, S., Yaguchi, J., Angerer, R. C., Angerer, L. M. and Burke, R. D.** (2010).

645   TGFβ signaling positions the ciliary band and patterns neurons in the sea urchin

646   embryo. *Dev. Biol.* **347**(1), 71-81. doi:10.1016/j.ydbio.2010.08.009

647

648

649
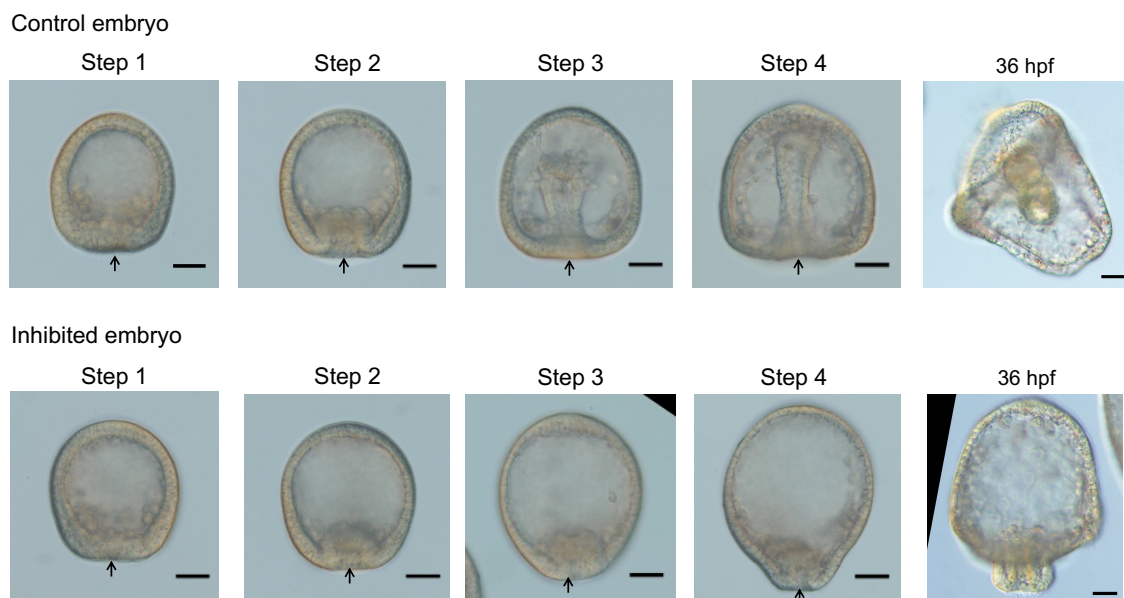
650

651

652

653

654

655   **Figures**

656

657

658   **Fig. 1. Developmental stages of control and H^+/K^+ ion pump-inhibited HP**

659   **embryos.** Typical bright-field images of the gastrulation process (steps 1-4) and 36 hpf

660   embryos (scale bars: 30 μm). Arrows indicate vegetal pole positions. Gastrulation did

661   not progress after step 2 in the inhibited embryos, and the outward protrusion of the

662   vegetal pole side was more pronounced at step 4. At 36 hpf, "partial" exogastrulation

663   was observed in the inhibited embryo.

664

665

666

667

668

669

670

671

672
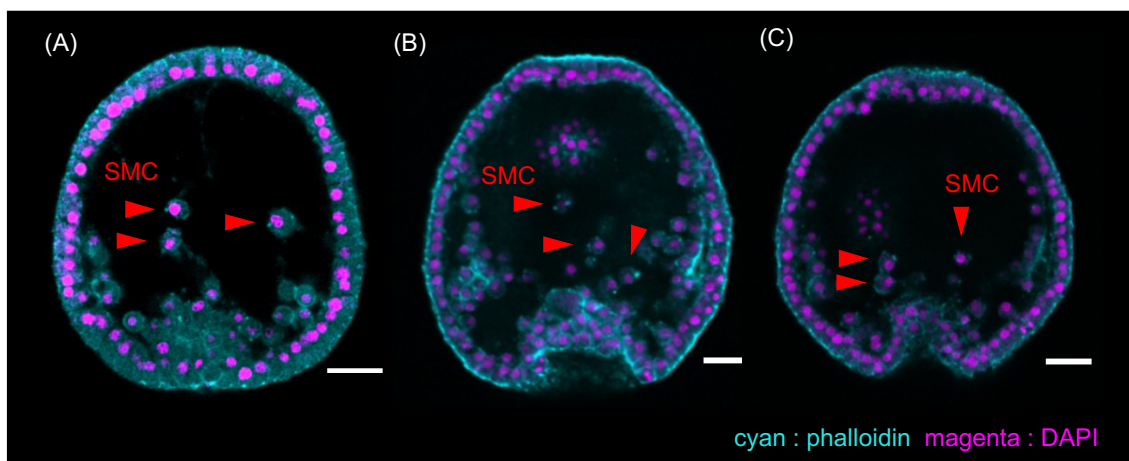
673

674 **Fig. 2. *In situ* SMC visualization of HP embryo development with inhibited H$^+$/K$^+$**

675 **ion pumps.** Confocal microscopy images at 24 hpf (A), 27 hpf (B), and 29 hpf (C)

676 (scale bars: 25 μm). The nucleus and F-actin in the embryos were stained with DAPI

677 (magenta) and phalloidin (cyan), respectively. SMC migration was confirmed at all

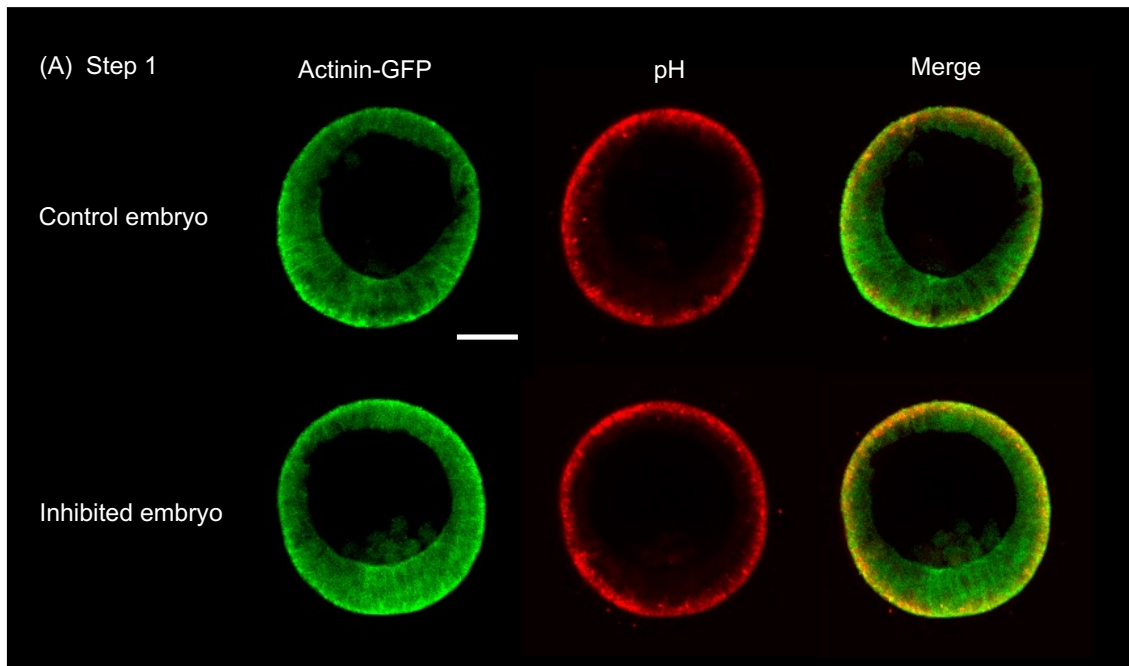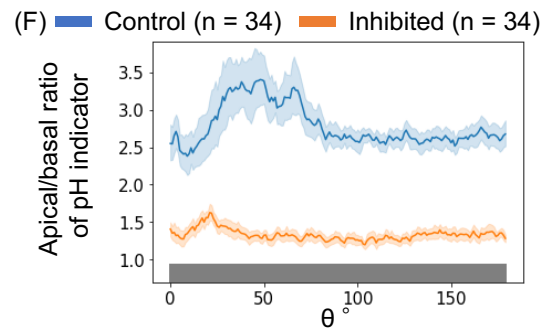678 developmental stages as indicated by red triangles.
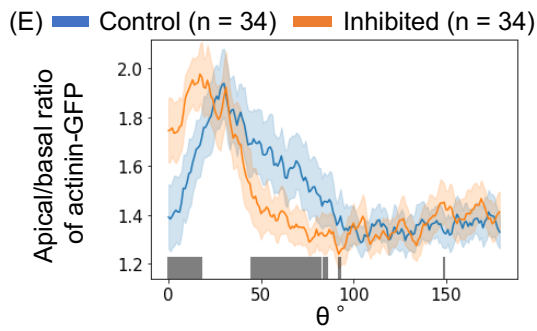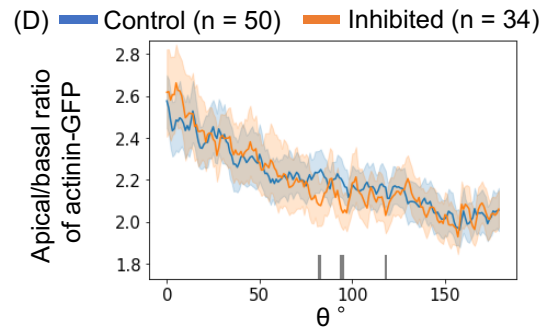
679

680

681

682

683

684

685

686

687

(B) Step 2 Actinin-GFP   pH   Merge

Control embryo

Inhibited embryo

688

(C)

180°
Animal Pole
90°
θ°
Vegetal Pole
0°

(D) Control (n = 50)   Inhibited (n = 34)

Apical/basal ratio
of actinin-GFP
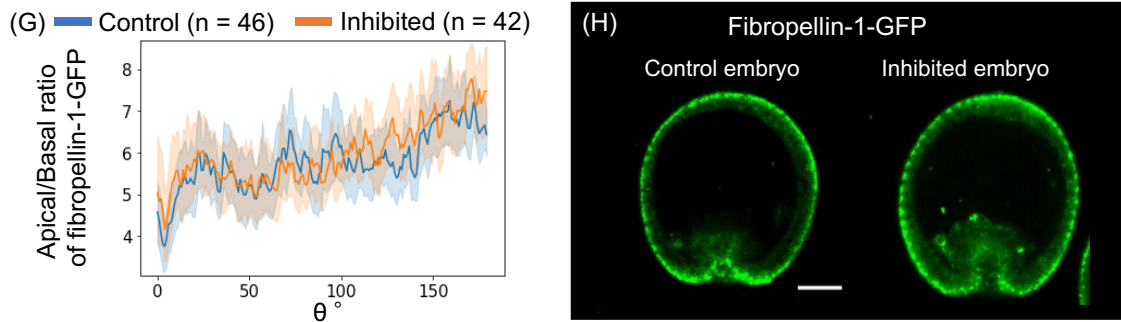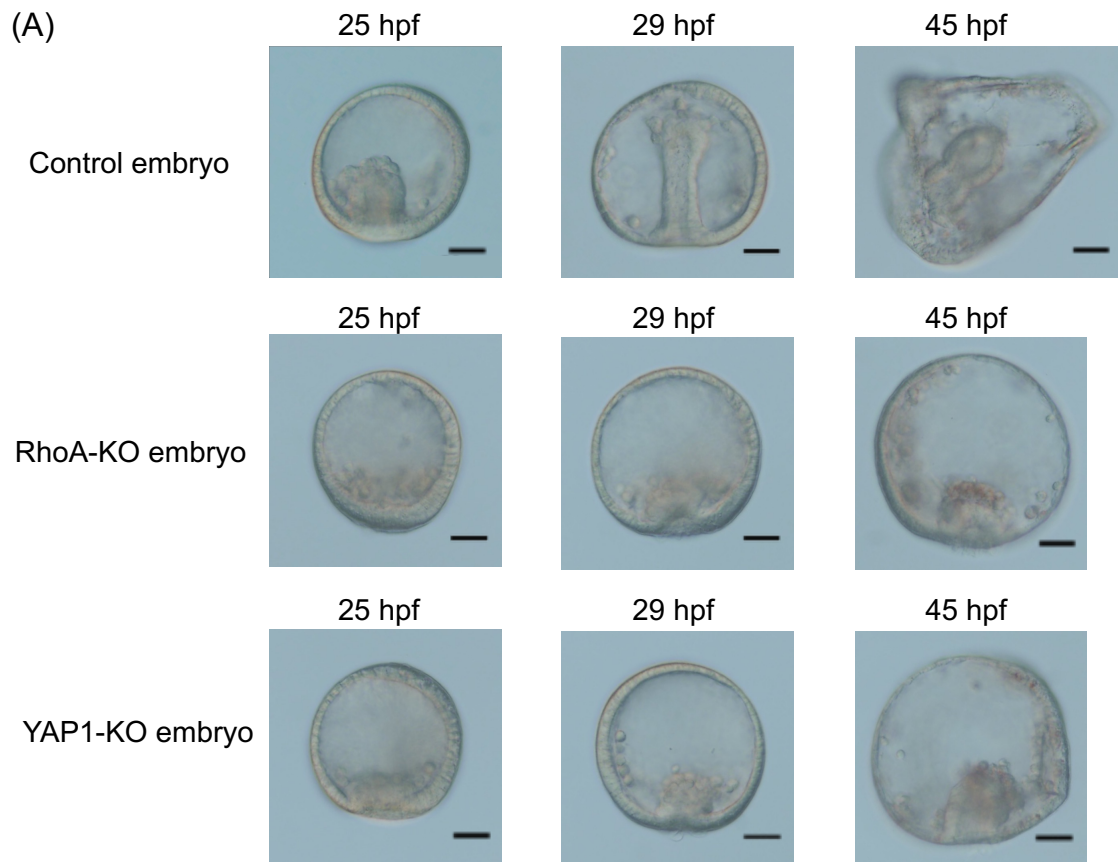
689

690

35
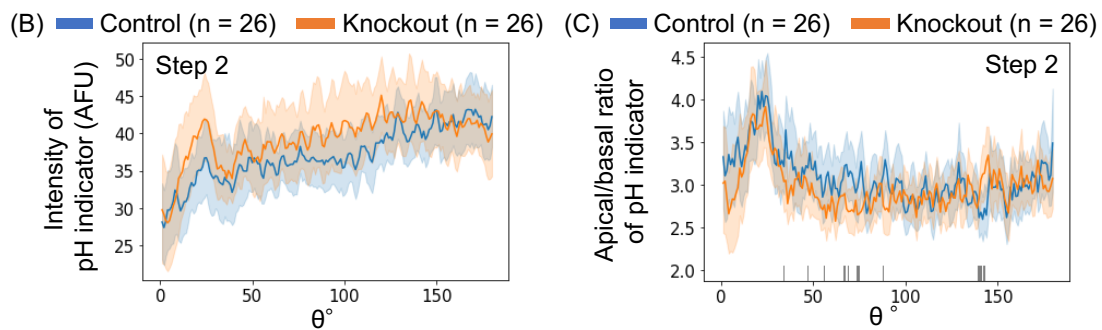
691
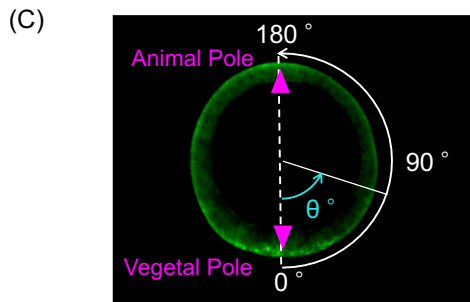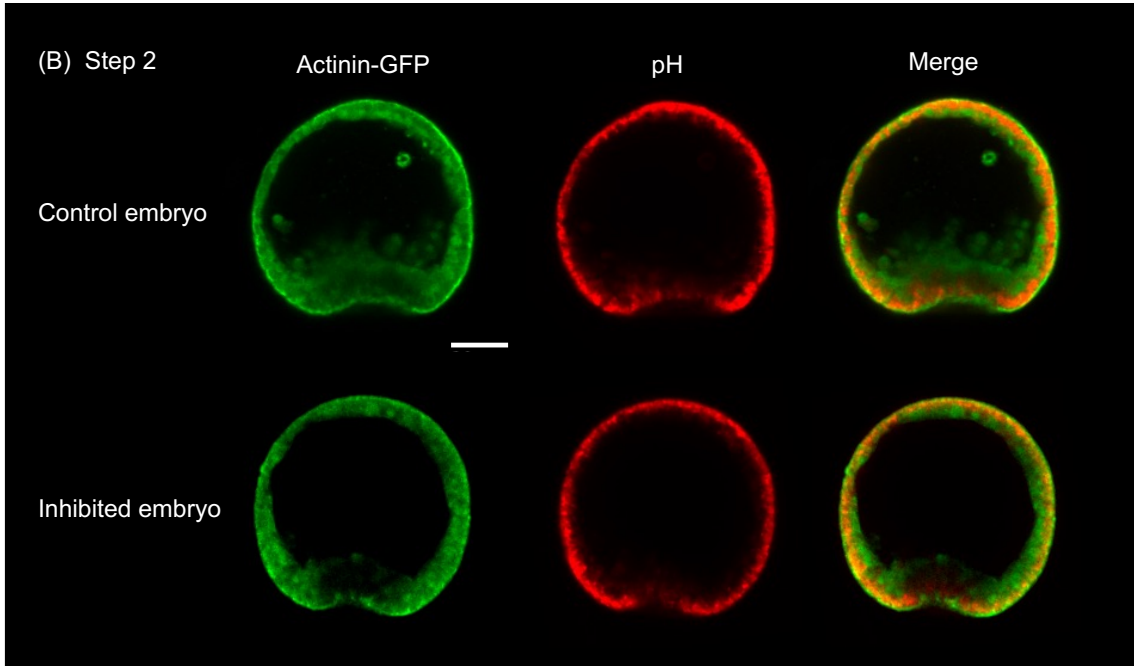
Fig. 3. Whole embryonic distributions of pH, actinin-GFP, and fibropellin-1-GFP.

(A-B) Confocal fluorescence microscopy images of co-stained intracellular pH (pH

indicator: red) and actinin (actinin-GFP: green) at gastrulation step 1 (A) and step 2 (B)

on the cross-section of animal poles and vegetal poles of control and inhibited embryos

(scale bars: 30 μm). (C) Definition of angle θ (0°~180°) from the vegetal pole (0°) to

the animal pole (180°) along the circumference of the embryo cross-section. (D-F)

Average apical/basal ratios and 95% confidence intervals (error bars) at angle θ of

actinin-GFP intensities at step 1 (D) and step 2 (E), pH indicator intensities at step 2 (F),

and fibropellin-1-GFP intensities at step 2 (G). Blue and orange curves and bars

represent the control and inhibited embryo values, respectively. Gray bars indicate

significantly different average values between the control and inhibited embryos

according to Welch's t-test ($p < 0.05$) (see also Fig. S1.). The correlation coefficients of

apical/basal ratios between actinin-GFP intensities (E) and pH indicator intensities (F)

in control and inhibited embryos were 0.56 and 0.64, respectively. (H) Fluorescence

images of fibropellin-1-GFP from control and inhibited embryos at gastrulation step 2

(scale bars: 30 μm).

(A)

Control embryo — 25 hpf, 29 hpf, 45 hpf

RhoA-KO embryo — 25 hpf, 29 hpf, 45 hpf

YAP1-KO embryo — 25 hpf, 29 hpf, 45 hpf

708

(B) Control (n = 26) Knockout (n = 26) **(C)** Control (n = 26) Knockout (n = 26)

709

710 **Fig. 4. Effect of F-actin regulator knockout on gastrulation.**

711 (A) Bright-field images of gastrulation (steps 2-3) in control, *RhoA* knockout, and *YAP1*

712 knockout embryos at selected time-points. PMCs and pigment cells were observed in all

713 embryos suggesting that development did not stop. The knockout embryos did not form

714 the structure like prism larva observed at 45 hpf (step 3) in the control embryo (scale

715 bars: 30 μm). (B-C) Average fluorescence intensities (arbitrary fluorescence units) and

37

716   95% confidence intervals (error bars) of intracellular pH indicator (B) and apical/basal

717   ratio of pH indicator (C) of *RhoA* knockout embryos and control embryos as a function

718   of angle θ. The meanings of the colors and θ are stated in Fig. 3 and Fig. S1.

719
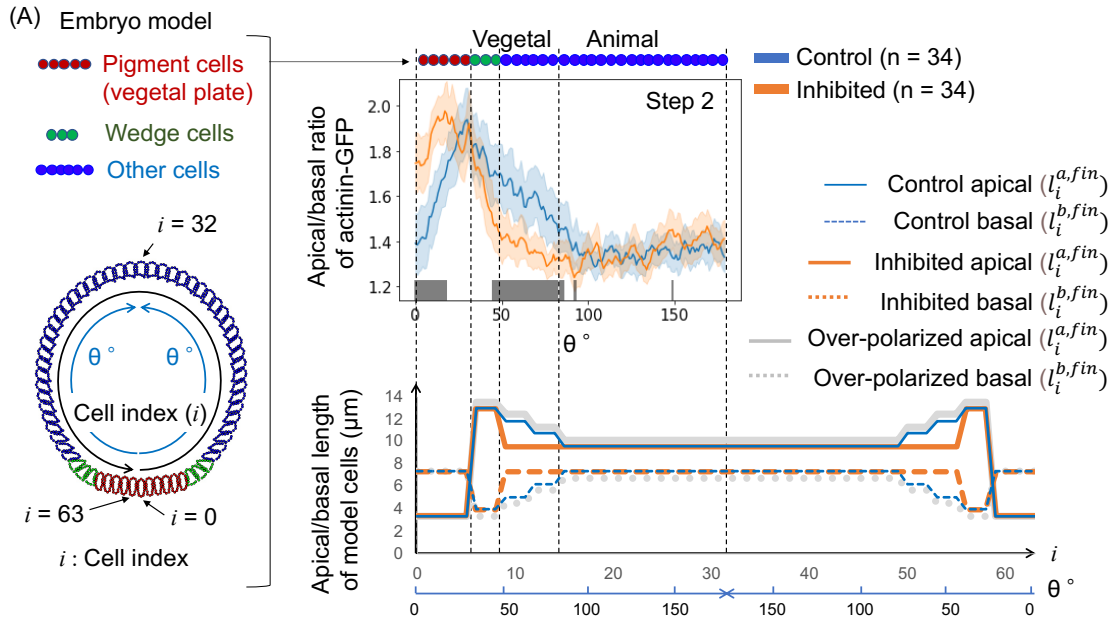
720

721
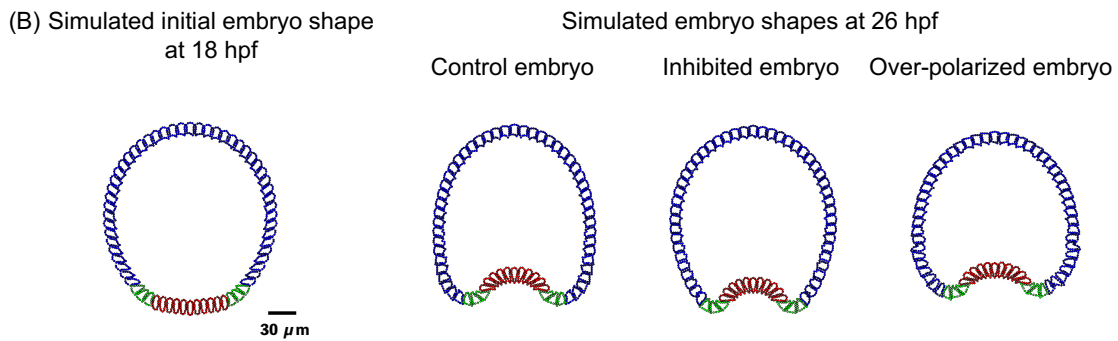
722

723
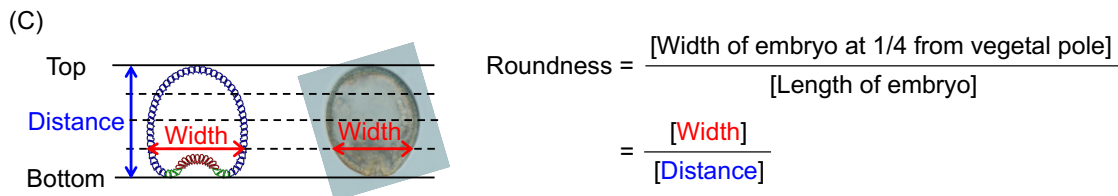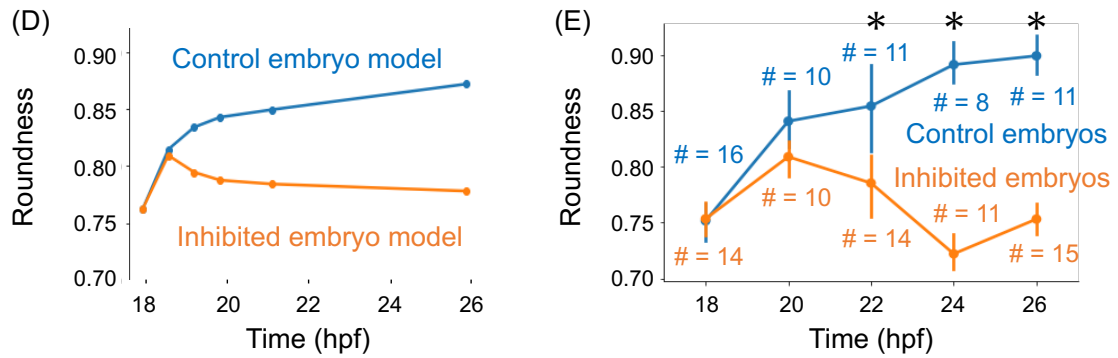
724

725

726

727

728

729

730

731

732

733

734

735

736

(A) Embryo model

Pigment cells (vegetal plate)

Wedge cells

Other cells

$i = 32$

$\theta\,°$ $\theta\,°$

Cell index (i)

$i = 63$ $i = 0$

i : Cell index

Vegetal   Animal

Control (n = 34)

Inhibited (n = 34)

Step 2

Apical/basal ratio of actinin-GFP

$\theta\,°$

Control apical ($l_i^{a,fin}$)

Control basal ($l_i^{b,fin}$)

Inhibited apical ($l_i^{a,fin}$)

Inhibited basal ($l_i^{b,fin}$)

Over-polarized apical ($l_i^{a,fin}$)

Over-polarized basal ($l_i^{b,fin}$)

Apical/basal length of model cells (μm)

i

$\theta\,°$

737

(B) Simulated initial embryo shape at 18 hpf

Simulated embryo shapes at 26 hpf

Control embryo   Inhibited embryo   Over-polarized embryo

30 μm

738

(C)

Top

Distance

Width   Width

Bottom

Roundness = [Width of embryo at 1/4 from vegetal pole] / [Length of embryo]

= [Width] / [Distance]

739

(D)

Roundness

Control embryo model

Inhibited embryo model

Time (hpf)

(E)

Roundness

= 16   # = 10   # = 11   # = 8   # = 11

= 14   # = 10   # = 14   # = 11   # = 15

Control embryos

Inhibited embryos

Time (hpf)

740

741   **Fig. 5. Coarse-grained model and simulation of control, inhibited, and over-**

742   **polarized embryos.** (A) Modeled cell lengths of apical and basal sides of control,

743   inhibited, and over-polarized embryos; $l_i^{a,fin}$ and $l_i^{b,fin}$ refer to the final length of the

744   apical and basal sides of the *i*-th cell, respectively (see Materials and methods).

745   Distributions of the final length of the former two models was determined based on the

746   distributions of apical/basal ratios of actinin-GFP intensities from control and inhibited

747   embryos in step 2. The top center panel was a modification of Fig. 3D. Red, green, and

748   blue circles in the top panel and panel (B) represent pigment cells, wedge cells, and

749   other cells, respectively. (B) Snapshots of the initial embryo shape at 18 hpf and at 26

750   hpf of the three models. (C) Definition of the roundness of the vegetal side of embryos

751   from simulation results and imaging. (D-E) Roundness indices of vegetal sides of

752   modeled control and inhibited embryos (D) and experimentally determined values (E).

753   Blue and orange # refer to the number of control and inhibited embryos at each time

754   point, error bars indicated 95% confidence intervals, and * indicated that the roundness

755   of control embryos was significantly larger than that of inhibited embryos according to

756   Welch's t-test ($p < 0.05$, see Fig. S4B).